Current issues in cumulus parameterization

Steven K. Krueger

Dept. of Meteorology, University of Utah, Salt Lake City, Utah

1. Introduction

In this chapter, I will first provide a brief introduction to cumulus parameterization and an overview of current issues in cumulus parameterization, followed by descriptions of the mass-flux formulation of cumulus parameterization, the effects of upper tropospheric stratiform clouds generated by cumulus detrainment, the diurnal cycle of deep cumulus convection, and some aspects of cumulus parameterization as the horizontal grid size decreases.

1.1 Background

Cumulus convection consists of narrow, saturated updrafts (i.e., cumulus or cumulonimbus clouds), narrow, nearly saturated precipitation-driven downdrafts, and broad, unsaturated downdrafts in the region surrounding the clouds. Cumulus convection occurs when the atmosphere is conditionally unstable (i.e., unstable with respect to moist adiabatic parcel displacements, but stable to dry adiabatic displacements). Cumulus convection may be organized into mesoscale convective systems, such as squall lines. The horizontal and vertical scales of cumulus *updrafts* are comparable. They range from a few hundred meters for shallow cumuli to several kilometers for deep cumulonimbi. Typical horizontal and vertical grid sizes in large-scale models (LSMs) used for numerical weather prediction (NWP) are about 50 km and 500 m, respectively, while in global climate models (GCMs), they are around 250 km and 1000 m. In such models, a cumulus updraft would extend through (or penetrate) one or more model layers, but would be horizontally subgrid-scale (SGS). This means that individual cumulus updrafts cannot be resolved by a LSM, and that a *cumulus parameterization* is required to represent their (collective) effects.

In terms of the global energy balance, the role of cumulus convection is to heat the troposphere. It does this by transporting energy, primarily in the form of latent heat (i.e., water vapor), vertically from the boundary layer to the free troposphere where it is converted to sensible heat by condensation. Because cumulonimbus clouds produce precipitation that usually reaches the surface, the net effect of an ensemble of such clouds is to heat the atmosphere.

Globally, the heating by cumulus convection nearly balances the net radiative cooling of the troposphere. This global state is referred to as *radiative-convective equilibrium*. Without cumulus convection, a purely radiative equilibrium would prevail. However, such an equilibrium state is absolutely unstable (i.e., it is unstable to dry adiabatic displacements), so it does not occur. Thus, at the most fundamental level, a cumulus parameterization must, in conjunction with suitable parameterizations of radiative transfer, boundary layer turbulent transport, and clouds, be able to reproduce the observed vertical thermodynamic structure of the troposphere.

1.2 Overview of current issues in cumulus parameterization

Over the Earth, cumulus convection tends to occur more frequently in certain regions, at certain times of the day and year, and under certain large-scale conditions. This suggests that a basic task of a cumulus parameterization in a GCM is to reproduce the observed global distribution of cumulus convection. Deep, precipitating cumulus convection commonly produces extensive upper tropospheric stratiform clouds that significantly affect radiation.

Therefore, an important goal of a cumulus parameterization is to determine the occurrence and properties of these clouds. The atmospheric boundary layer can be strongly affected by cumulus convection, so a cumulus parameterization should represent the relevant processes. It is also becoming increasingly common for cumulus parameterizations in GCMs to estimate the cumulus effects on the large-scale horizontal momentum, and even on the large-scale chemistry of various chemical species.

One of the primary goals of NWP is to accurately predict precipitation. During the summer over continents, much of the precipitation is convective. Therefore, it would be desirable for the cumulus parameterization in a NWP model to be able to determine precisely when and where cumulus convection will occur. The diurnal cycle plays an important role in determining when and where convective precipitation occurs, especially over land. This often involves destabilization and triggering due to local boundary layer processes (surface fluxes, gust fronts). In addition, diurnally forced mesoscale circulations, such as sea and land breezes and mountain-plains circulations, may trigger or suppress convection via low-level mesoscale ascent or descent.

In general, the cumulus parameterizations currently used in GCMs and NWP models consist of a model of the cumulus ensemble effects on the large-scale budget equations, a cumulus ensemble model, and closure assumptions. All three aspects use the concept of *cumulus mass flux* in their formulations.

In addition, the occurrence of cumulus convection must be diagnosed. This is often called "triggering". Triggering is determined by the relative effects of processes that tend to inhibit convection and those that tend to promote it. It becomes more important (and difficult) to diagnose as the horizontal grid size of the LSM decreases.

2. Mass-flux formulation of cumulus parameterization

2.1 Effects of a cumulus ensemble upon the large-scale temperature and moisture fields by induced subsidence and detrainment

By 1970, meteorologists had begun to recognize the importance of cumulus-induced subsidence and detrainment of cloud air in modifying the large-scale environment. Arakawa and Schubert (1974) proposed a theory for the interaction of a cumulus ensemble with the large-scale environment in which the roles of mass flux in the cumulus ensemble and detrainment from the clouds were explicitly included. In this section, we will derive these effects using the mass-flux formulation for the simplified situation in which all clouds have the same thermodynamic characteristics at each level. In other words, we will assume that there is only a single cloud type. Arakawa and Schubert used the more realistic assumption that cumulus clouds of several types can co-exist.

(a) Preliminary considerations

For convenience, we define the *dry static energy* as

$$s \equiv c_p T + gz, \tag{1}$$

and the moist static energy as

$$h \equiv c_p T + gz + Lq, \tag{2}$$

where s is the sum of enthalpy and potential energy, and h the sum of s and latent energy. For dry adiabatic processes,

$$\frac{ds}{dt} \approx 0, \tag{3}$$

while for both dry and moist adiabatic processes,

$$\frac{dh}{dt} \approx 0, \tag{4}$$

We consider an ensemble of cumulus clouds that is embedded in a tropical large-scale motion system. The thermodynamic energy equation is

$$\frac{ds}{dt} = Q_r + L(c-e), \tag{5}$$

where Q_R is the radiative heating rate, c the rate of condensation, e the rate of evaporation of cloud condensate per unit mass of air. The continuity equation for moisture is

$$\frac{dq}{dt} = e - c. \tag{6}$$

With the aid of the (anelastic) continuity equation,

$$\nabla_h \cdot (\rho \mathbf{V}_h) + \frac{\partial(\rho w)}{\partial z} = 0, \tag{7}$$

(5) and (6) are written in the flux forms

$$\frac{\partial(\rho s)}{\partial t} + \nabla_h \cdot (\rho s \mathbf{V}_h) + \frac{\partial(sm)}{\partial z} = \rho Q_R + \rho L(c-e), \tag{8}$$

$$\frac{\partial(\rho q)}{\partial t} + \nabla_h \cdot (\rho q \mathbf{V}_h) + \frac{\partial(qm)}{\partial z} = \rho(e-c), \tag{9}$$

where $m \equiv \rho w$ is the *vertical mass flux* per unit area.

We consider a horizontal area that is large enough to contain an ensemble of cumulus clouds but small enough to be regarded as a fraction of a large-scale motion system. Taking horizontal averages of (8) and (9), we obtain

$$\frac{\partial(\rho s)}{\partial t} + \nabla_h \cdot \left(\overline{\rho s \mathbf{V}_h}\right) + \frac{\partial(\overline{sm})}{\partial z} = \rho \bar{Q}_R + \rho L(\overline{c-e}) - \frac{\partial(\overline{s'm'})}{\partial z}, \tag{10}$$

$$\frac{\partial(\rho \bar{q})}{\partial t} + \nabla_h \cdot \left(\overline{\rho q \mathbf{V}_h}\right) + \frac{\partial(\overline{qm})}{\partial z} = \rho(\overline{e-c}) - \frac{\partial(\overline{q'm'})}{\partial z}, \tag{11}$$

where the $\overline{(\ )}$ is the horizontal average, and $(\ )'$ is the deviation from the average.

Let σ be the fractional area occupied by active cumulus clouds at a particular level. Then $\sigma = \sum_i \sigma_i$, where σ_i is the fractional area covered by the ith cloud. For simplicity, we assume that *all clouds have the same characteristic values of s, q, and ρw at a given level.* Then

$$\begin{aligned} \bar{s} &= \sigma s_c + (1-\sigma)\tilde{s} \\ \bar{q} &= \sigma q_c + (1-\sigma)\tilde{q} \end{aligned} \tag{12}$$

$$\begin{aligned}\bar{m} &\equiv \overline{\rho w} = \sigma m_c + (1-\sigma)\tilde{m}, \\ &= M_c + \tilde{M}.\end{aligned} \tag{13}$$

M_c is called the *cloud mass flux*, $(\,)_c$ is the in-cloud value, and $\tilde{(\,)}$ is the value in the cloud-free environment.

$$\overline{sm} = \sigma s_c m_c + (1-\sigma)\tilde{s}\tilde{m},$$
$$\overline{sm} = \sigma^2 s_c m_c + (1-\sigma)^2 \tilde{s}\tilde{m} + \sigma(1-\sigma)(\tilde{s}m_c + s_c\tilde{m})$$

Therefore

$$\begin{aligned}\overline{s'm'} &= \overline{sm} - \bar{s}\,\bar{m} \\ &= \sigma(1-\sigma)(s_c - \tilde{s})(m_c - \tilde{m}).\end{aligned} \tag{14}$$

We will make use of the facts:

$$\sigma << 1 \tag{15a}$$

$$|s_c - \tilde{s}| << \tilde{s}, \quad |q_c - \tilde{q}| << \tilde{q} \tag{15b}$$

[(15b) are strong (sufficient) conditions. They are not necessary.] Then we obtain

$$\begin{aligned}\bar{s} &= \sigma(s_c - \tilde{s}) + \tilde{s} \approx \tilde{s} \\ \bar{q} &= \sigma(q_c - \tilde{q}) + \tilde{q} \approx \tilde{q}\end{aligned} \tag{16}$$

However, $\bar{m}$ (mean large-scale vertical mass flux) $\neq \tilde{m}$ (vertical mass flux of the cloud environment).

(Case 1):

$$\bar{m} = 0 \text{ (no net vertical mass flux)}$$

$$\tilde{m} = -\frac{\sigma}{1-\sigma} m_c \text{ (compensating downward mass flux)}$$

Therefore

$$m_c - \tilde{m} = m_c\left(1 + \frac{\sigma}{1-\sigma}\right) = \frac{m_c}{1-\sigma},$$

and (exact)

$$\overline{s'm'} = \sigma m_c(s_c - \tilde{s} = M_c(s_c - \tilde{s}). \tag{17a}$$

(Case 2):

$$\begin{aligned}&\tilde{m} = 0 \quad \text{(all ascent is in clouds only)} \\ &\overline{s'm'} = \sigma m_c(1-\sigma)(s_c - \tilde{s}) \approx M_c(s_c - \tilde{s})\end{aligned} \tag{17b}$$

Therefore in general we have

$$\overline{s'm'} \approx \sigma m_c(s_c - \tilde{s}) = M_c(s_c - \tilde{s}). \tag{18}$$

Therefore (10) and (11) become

$$\frac{\partial(\rho\bar{s})}{\partial t}+\nabla_h\cdot(\overline{\rho s\mathbf{V}_h})+\frac{\partial(\bar{s}\ \bar{m})}{\partial z}=\rho Q_R+\rho L(c-e)-\frac{\partial}{\partial z}[M_c(s_c-\tilde{s})], \tag{19}$$

(apparent heat source)

$$\frac{\partial(\rho\bar{q})}{\partial t}+\nabla_h\cdot(\overline{\rho q\mathbf{V}_h})+\frac{\partial(\overline{qm})}{\partial z}=\rho(e-c)-\frac{\partial}{\partial z}[M_c(q_c-\tilde{q})], \tag{20}$$

(apparent moisture source)

where the $\overline{(\ )}$ symbol has been omitted for Q_R, c, and e. From (19) and (20) we have also

$$\frac{\partial(\rho\bar{h})}{\partial t}+\nabla_h\cdot(\overline{\rho h\mathbf{V}_h})+\frac{\partial(\bar{h}\bar{m})}{\partial z}=\rho Q_R-\frac{\partial}{\partial_z}\left[M_c(h_c-\tilde{h})\right] \tag{21}$$

where $h = s + Lq$ (moist static energy).

2.2 The effects of cumulus-induced subsidence and detrainment

So far we have expressed the vertical cumulus transports of sensible heat and moisture in terms of the cloud mass flux M_c and the excess of s_c (thus T_c) and q_c from the environmental values.

For simplicity let us ignore the radiative heating Q_R and evaporation of clouds e. Then (19) and (20) are simplified as

$$\frac{\partial(\rho\bar{s})}{\partial t}+\nabla_h\cdot(\overline{\rho s\mathbf{V}_h})+\frac{\partial(\bar{s}\ \bar{m})}{\partial z}=\rho Lc-\frac{\partial}{\partial z}[M_c(s_c-\tilde{s})] \tag{22}$$

$$\frac{\partial(\rho\bar{q})}{\partial t}+\nabla_h\cdot(\overline{\rho q\mathbf{V}_h})+\frac{\partial(\overline{qm})}{\partial z}=-\rho c-\frac{\partial}{\partial z}[M_c(q_c-\tilde{q})] \tag{23}$$

We assume that *the cumulus ensemble maintains a heat and moisture balance with the large-scale environment. Thus there will be no accumulation of heat or moisture in the cumulus ensemble over a time scale describing the large-scale motion.* The balance equations for the cumulus ensemble are:

$$\frac{\partial(\rho\sigma s_c)}{\partial t}=\frac{\partial M_c}{\partial z}\tilde{s}-\frac{\partial(M_c s_c)}{\partial z}+\rho Lc=0, \text{ (heat balance)} \tag{24}$$

$$\frac{\partial(\rho\sigma q_c)}{\partial t}=\frac{\partial M_c}{\partial z}\tilde{q}-\frac{\partial(M_c q_c)}{\partial z}-\rho c=0, \text{ (moisture balance)} \tag{25}$$

$$\frac{\partial(\rho\sigma h_c)}{\partial t}=\frac{\partial M_c}{\partial z}\tilde{h}-\frac{\partial(M_c h_c)}{\partial z}=0, \text{ (moist static energy balance)} \tag{26}$$

for the entrainment layer where $\partial M_c/\partial z > 0$ and

$$\frac{\partial(\rho\sigma s_c)}{\partial t}=\frac{\partial M_c}{\partial z}s_c-\frac{\partial(M_c s_c)}{\partial z}+\rho Lc=0 \tag{27}$$

$$\frac{\partial(\rho\sigma q_c)}{\partial t}=\frac{\partial M_c}{\partial z}q_c-\frac{\partial(M_c q_c)}{\partial z}-\rho c=0 \tag{28}$$

$$\frac{\partial(\rho\sigma h_c)}{\partial t} = \frac{\partial M_c}{\partial z} h_c - \frac{\partial(M_c h_c)}{\partial z} = 0 \tag{29}$$

for the detrainment layer where $\partial M_c / \partial z < 0$.

- For the entrainment layer, we substitute (25) into the right-hand side of (22) to find

$$\begin{aligned} \rho Lc - \frac{\partial}{\partial z}[M_c(s_c - \tilde{s})] &= L\left[\frac{\partial M_c}{\partial z}\tilde{q} - \frac{\partial(M_c q_c)}{\partial z}\right] - \frac{\partial}{\partial z}[M_c(s_c - \tilde{s})] \\ &= \frac{\partial M_c}{\partial z} L\tilde{q} - \frac{\partial(M_c h_c)}{\partial z} + \frac{\partial(M_c \tilde{s})}{\partial z} \\ &= \frac{\partial M_c}{\partial z}\tilde{h} - \frac{\partial(M_c h_c)}{\partial z} + M_c \frac{\partial \tilde{s}}{\partial z} \\ &= M_c \frac{\partial \tilde{s}}{\partial z} \end{aligned} \tag{30}$$

Therefore (22) becomes

$$\frac{\partial(\rho\bar{s})}{\partial t} + \nabla_h \cdot (\overline{\rho s \mathbf{V}_h}) + \frac{\partial(\overline{sm})}{\partial z} = M_c \frac{\partial \tilde{s}}{\partial z} \tag{31}$$

Similarly (23) becomes

$$\frac{\partial(\rho\bar{q})}{\partial t} + \nabla_h \cdot (\overline{\rho q \mathbf{V}_h}) + \frac{\partial(\overline{qm})}{\partial z} = M_c \frac{\partial \tilde{q}}{\partial z} \tag{32}$$

- For the detrainment layer $\partial M_c / \partial z < 0$, we obtain from (29) that

$$M_c \frac{\partial h_c}{\partial z} = 0. \tag{33}$$

If we substitute (28) into the right-hand side of (22) we find

$$\begin{aligned} \rho Lc - \frac{\partial}{\partial z}[M_c(s_c - \tilde{s})] &= L\left[\frac{\partial M_c}{\partial z} q_c - \frac{\partial(M_c q_c)}{\partial z}\right] - \frac{\partial}{\partial z}[M_c(s_c - \tilde{s})] \\ &= -LM_c \frac{\partial q_c}{\partial z} - M_c \frac{\partial s_c}{\partial z} + M_c \frac{\partial \tilde{s}}{\partial z} - (s_c - \tilde{s}) \frac{\partial M_c}{\partial z} \\ &= -M_c \frac{\partial h_c}{\partial z} + M_c \frac{\partial \tilde{s}}{\partial z} - (s_c - \tilde{s}) \frac{\partial M_c}{\partial z} \\ &= M_c \frac{\partial \tilde{s}}{\partial z} - (s_c - \tilde{s}) \frac{\partial M_c}{\partial z} \end{aligned} \tag{34}$$

Therefore (22) becomes

$$\frac{\partial(\rho\bar{s})}{\partial t} + \nabla_h \cdot (\overline{\rho s \mathbf{V}_h}) + \frac{\partial(\overline{sm})}{\partial z} = M_c - \frac{\partial \tilde{s}}{\partial z} - (s_c - \tilde{s}) \frac{\partial M_c}{\partial z} \tag{35}$$

Similarly (23) becomes

$$\frac{\partial(\rho\bar{q})}{\partial t} + \nabla_h \cdot (\overline{\rho q \mathbf{V}_h}) + \frac{\partial(\overline{qm})}{\partial z} = M_c - \frac{\partial \tilde{q}}{\partial z} - (q_c - \tilde{q}) \frac{\partial M_c}{\partial z} \tag{36}$$

For the entrainment layer, (31) shows that the apparent heating (in the absence of radiative heating and evaporative cooling) is due to the *adiabatic (compression) warming by the downward motion between the clouds, which is compensating the cumulus mass flux* $M_c(M_c\partial\tilde{s}/\partial z>0)$.

Equation (32) shows that the apparent moisture sink is due to the drying effect of the compensating subsidence $(M_c\partial\tilde{q}/\partial z>0)$.

In addition, for the detrainment layer, (35) and (36) show that the detrainment of excess static energy, $s_c-\tilde{s}=c_p(T_c-\tilde{T})$, and excess moisture, $q_c-\tilde{q}$, act to warm (if $T_c-\tilde{T}>0$) and moisten (if $q_c-\tilde{q}>0$) the environment.

In this simple case, the problem of parameterization of cumulus convection reduces to the *determination of* M_c *in terms of the large-scale variables*. Once M_c is known, we can obtain h_c from (26). Then using the relations

$$s_c-\tilde{s}=c_p(T_c-\tilde{T})=\frac{1}{1+\gamma}(h_c-\tilde{h}^*), \tag{37a}$$

$$q_c-\tilde{q}^*=\frac{1}{1+\gamma}\frac{1}{L}(h_c-\tilde{h}^*), \tag{37b}$$

where

$$\gamma\equiv\frac{L}{c_p}\left(\frac{\partial\tilde{q}^*}{\partial\tilde{T}}\right)_p$$

we can determine T_c and q. In the above, $\tilde{q}^*(\tilde{T},p)$ is the saturation mixing ratio at $(\tilde{T},p)$, and $\tilde{h}^*\equiv\tilde{s}+L\tilde{q}^*$ is the saturation moist static energy. The rate of condensation c is determined by (25), because we know M_c and q_c in addition to $\tilde{q}$ $(\approx\overline{q})$.

Let us examine the physical meaning of (31). For simplicity we consider a special case where $\nabla_h\tilde{s}\approx\nabla_h\overline{s}=0$. Then (31) becomes

$$\frac{\partial(\rho\overline{s})}{\partial t}+\overline{m}\frac{\partial\overline{s}}{\partial z}=M_c\frac{\partial\tilde{s}}{\partial z}\approx M_c\frac{\partial\overline{s}}{\partial z}, \tag{38}$$

where we have used (7) and $\overline{\rho s'\mathbf{V}'_h}\approx 0$. In order that warming of the large-scale environment is to occur, we must have

$$M_c>\overline{m} \tag{39}$$

or

$$\overline{m}<0 \quad \text{[see (13)]} \tag{39a}$$

Therefore M_c *must exceed the mean vertical mass flux required from the large-scale convergence, and the vertical motion outside of the clouds is necessarily downward.*

2.3 The closure assumption for the Arakawa-Schubert cumulus parameterization

In the Arakawa-Schubert (AS) cumulus parameterization, (Arakawa and Schubert, 1974; Lord and Arakawa, 1980), closure is achieved by assuming that a balance exists between the generation of moist convective instability and its destruction by clouds as shown schematically in Fig. 2.1. To provide a physical interpretation of the closure assumption, let's look at the cumulus ensemble kinetic energy budget for the case of an ensemble consisting of a single cloud type, as assumed in sections (2.1) and (2.2). Let K be the cloud-scale kinetic energy for the ensemble, A be the cloud work function defined as the cloud-scale kinetic energy generation per unit ensemble cloud-base mass flux, M_B, and D be the cloud-scale kinetic energy dissipation rate per unit M_B. The kinetic energy budget for the ensemble may be written as

$$\frac{dK}{dt} = (A - D)M_B \tag{40}$$

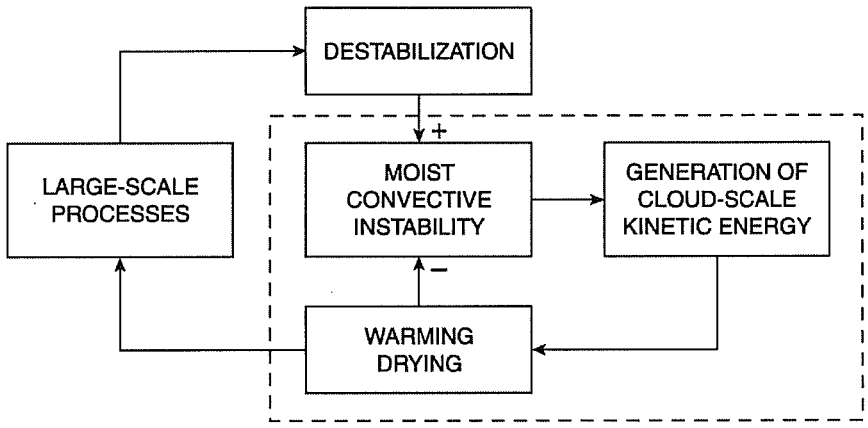

Figure 2.1 A schematic diagram of the Arakawa-Schubert closure assumption. The dashed line represents the cumulus parameterization. [From Lord and Arakawa (1980). Reprinted with permission from the American Meteorological Society.]

When there is no generation of kinetic energy, only dissipation will act on the ensemble. Let τ_{DIS} be the decay time in this situation. Then, in terms of order of magnitude (40) gives

$$DM_B \sim \frac{K}{\tau_{DIS}} \tag{41}$$

Let τ be the time scale over which we apply (40). Then using (42) in (40) we have

$$\frac{K}{\tau} \sim AM_B - \frac{K}{\tau_{DIS}} \tag{42}$$

When $\tau >> \tau_{DIS}$ the left-hand side of (42), and therefore of (40), can be neglected. Eq. (40) then gives

$$A = D \text{ for } M_B > 0 \tag{43}$$

This equation states the "kinetic energy quasi-equilibrium" for the ensemble.

τ_{DIS} must be smaller than a cloud lifetime which includes both generation and dissipation. This means τ_{DIS} is of the order of 10^2 to 10^3 s. An appropriate choice of τ would be the time scale of a large-scale disturbance, τ_{LS}, where τ_{LS} is typical of the order 10^5 s. Then $\tau_{DIS} << \tau_{LS}$, and the kinetic energy quasi-equilibrium is a very good approximation.

The primary source of kinetic energy generation for cumulus convection is the buoyancy force. Therefore, the cloud work function A was defined by Arakawa and Schubert (1974) as the ensemble kinetic energy generation (per unit cloud-base mass flux) due to work by the buoyancy force, i.e.,

$$A = \int_{z_B}^{\hat{z}} \frac{g}{\overline{T}(z)} \eta(z) \left[T_{vc}(z) - \overline{T}_v(z) \right] dz \tag{44}$$

where $T_{vc}(z)$ and $\overline{T}_v(z)$ are the ensemble and environmental virtual temperatures, $\hat{z}$ is the ensemble cloud-top height, and $\eta(z)$ is the ensemble normalized vertical mass flux. When the cloud is non-entraining, $\eta(z) = 1$, and A is equal to the convective available potential energy (CAPE).

In general, the total dissipation should be roughly proportional to the cloud mass flux. Then D, which is the dissipation *per unit cloud-base mass flux*, will not depend on the large-scale situation for a particular cloud type. It is quasi-constant for each cloud type.

To derive a practical closure assumption, one takes the derivative of (43) with respect to a time long enough for the kinetic energy quasi-equilibrium to hold. Then,

$$\frac{dA}{dt} = \frac{dD}{dt}. \tag{45}$$

Based on the above argument, one may set

$$\frac{dD}{dt} = 0, \tag{46}$$

even when the cumulus ensemble is not in an exactly steady state. Then, from (45),

$$\frac{dA}{dt} = 0 \tag{47}$$

This constraint on A can be used as a closure assumption, as follows.

One separates dA/dt into two parts, one representing the cumulus feedback on the large-scale fields, and the other representing the effects of the large-scale processes. Then (47) becomes

$$\left[\frac{dA}{dt} \right]_{CU} + \left[\frac{dA}{dt} \right]_{LS} = \left[\frac{dA}{dt} \right], \tag{48}$$

where the subscript "*CU*" refers to cumulus effects. We call $(dA/dt)_{LS}$ the "large-scale forcing," F. This can be divided into "cloud layer forcing," F_c, and "mixed layer forcing," F_M. The most dominant effect in the cloud layer forcing is the increase of the cloud work function due to cooling of the environment above the mixed layer by large-scale processes, typically by adiabatic cooling due to largescale upward motion. The mixed layer forcing includes the increase of the cloud work function through deepening of the mixed layer by large-scale horizontal convergence and by the upward flux of moist static energy at the surface. The diurnal cycle of cumulus convection over land is largely a consequence of the diurnal cycle of mixed layer forcing.

3. Upper tropospheric stratiform clouds generated by detrainment

Improved knowledge and understanding of upper tropospheric stratiform cloud generation, re-generation, and dissipation mechanisms are critical to the formulation and verification of methods to realistically capture these processes in regional and large-scale climate models. Relevant scientific questions include:

- How are the radiative, microphysical and spatial properties of cirrus anvils and associated cirrus cloud systems related to the precipitating deep convective cloud systems that produce them?

- How do the radiative properties, microphysical properties and spatial properties of such cloud systems evolve with time through the entire lifecycle of the cloud systems and what are the controlling factors in this evolution?

3.1 Observed structure and life cycle of tropical convective cloud systems

Much of the deep convection over the tropics occurs in cloud systems which consist of many individual cumulonimbus cells whose high-level outflow forms an extensive high cloud. In some cases, the cloud system may include a precipitating anvil cloud to the rear of the active cumulonimbus cells that is associated with a mesoscale updraft within the cloud and a mesoscale downdraft beneath it. Figure 3.1 from Houze (1977) illustrates the structure of this type of mesoscale convective system, which is referred to as a squall-line system. It consists of narrow line of deep convection and an extensive, trailing anvil region. The latter may be subdivided into a precipitating part (detectable by 5-cm radar), and non-precipitating part.

Leary and Houze (1979) described the structure and evolution of the precipitation area of a mesoscale convective system.In their formative stage, mesoscale precipitation features consist of a group of isolated cumulonimbus cells. In the intensifying stage, the rain areas of the individual cells merge. In the upper troposphere, an overhang of cloud and precipitation particles extends downwind in the layer of outflow from deep convective updrafts. The mature mesoscale precipitation area consists of both a region of convective cells and a large area of stratiform precipitation. The stratiform precipitation is maintained by mesoscale ascent in an anvil cloud extending from the mid to the upper troposphere. In the dissipating stage, convective cells cease forming, but the area of stratiform precipitation persists for at least several hours longer.

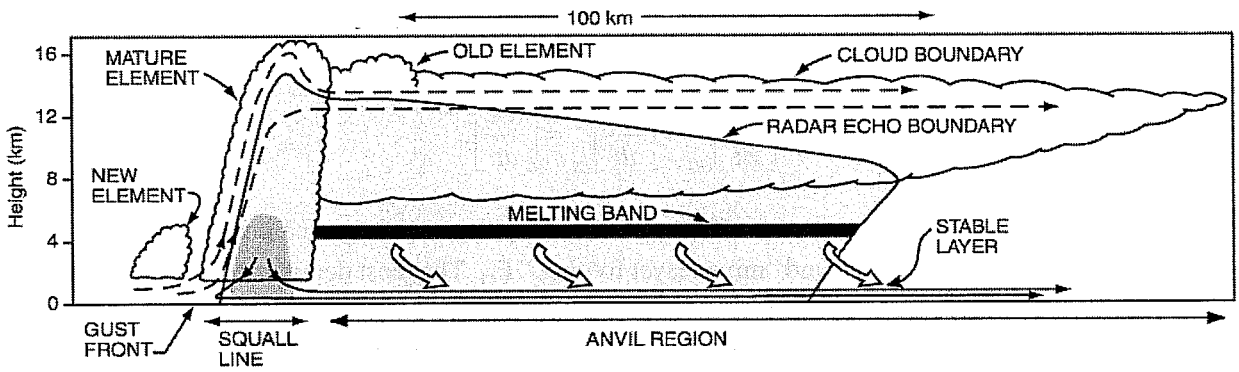

Figure 3.1 From Houze (1977). [Reprinted with permission from the American Meteorological Society.]

In contrast to the many radar-based studies of convective cloud systems that emphasized precipitation features, Machado and Rossow (1993) used satellite imagery to examine the properties of tropical convective cloud systems. Machado and Rossow determined the size distribution, average cloud properties, and their variation with cloud system size. Average convective cloud system properties suggest two major cloud types: one with lower

cloud-top pressures and much higher optical thicknesses, associated with deep convection, and one with higher cloud-top pressures and lower optical thicknesses, associated with the mesoscale stratiform anvil clouds. The anvil cloud properties show some evidence of a further division into optically thicker and thinner parts. The average properties of these clouds vary in a correlated fashion such that a larger horizontal extent of the convective system cloud is accompanied by a lower convective cloud-top pressure, larger anvil cloud size, and larger anvil cloud optical thickness. These structural properties and their diurnal variation also suggest that the smallest convective systems may represent a mixture of the formative and dissipating stages, while the medium and large sizes are, principally, the mature stage. Figure 3.2 (from Machado and Rossow) is a schematic of the life cycle of a convective system that is consistent with their results and previous studies of convective systems.

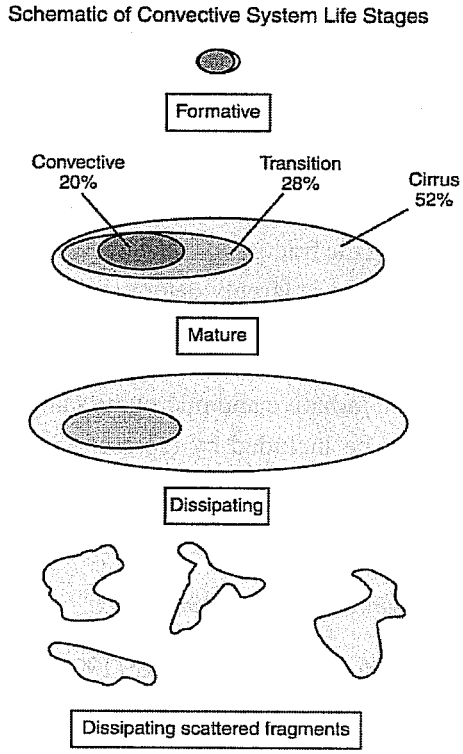

Figure 3.2 From Machado and Rossow (1993). [Reprinted with permission from the American Meteorological Society.]

In order to observationally link large-scale cloud patterns and atmospheric circulation, Lau and Crane (1995, 1997) produced composite cloud patterns from satellite and surface observations, while the concurrent three-dimensional atmospheric circulation was obtained from the operational analyses generated at the European Centre for Medium-Range Weather Forecasts (ECMWF). Their results for synoptic-scale tropical circulation systems in the tropical western Pacific Ocean show an area of high-top, thick, (precipitating) nimbostratus clouds in the region of ascending motion at 500 mb, trailed by an area of high-top, thin, (non-precipitating) altostratus/cirrus in a region of no significant vertical motion (Lau and Crane 1995, 1997). The composite cloud system is about 1500 km in extent.

3.2 Parameterization issues

Cloud-resolving modeling studies of thin, non-precipitating stratiform clouds (e.g., stratocumulus, altocumulus, and cirrus) have demonstrated the importance of radiative destabilization and the resulting shallow convection in the maintenance of such clouds. The strong coupling of small-scale physical processes makes parameterization of

such clouds in large-scale models challenging. CRMs, including LES models, have been successfully used to simulate many aspects of such thin stratiform clouds.

A unique aspect of convectively generated cirrus anvils is their origin from a concentrated source, at least in the case of isolated cumulonimbi that detrain directly into the cloud-free environment. In the case of convective cloud systems with a precipitating anvil, one may consider the source of cirrus to be more extensive, because much of the ice mass is generated in the precipitating anvil, and the cumulonimbi detrain into the precipitating anvil, not the clear environment. However, from a GCM perspective, these two types of convective cloud systems are often not distinguished because the precipitating anvil, and its mesoscale circulation, are sub-grid scale. In this case, all sub-grid scale circulations associated with a convective system, including the mesoscale circulation, are represented by the cumulus parameterization.

In GCMs, the radiative effects of convective cells are generally neglected, while those of the anvils are not. Not too long ago, presence of anvils was simply diagnosed based on the existence of deep convection. Now, with the widespread adoption of prognostic cloud water/ice schemes, anvils are represented as a source term due to detrainment from deep cumulus convection. However, even with prognostic cloud water/ice schemes, there remains the difficult problem of determining the fractional cloud cover at each level. It should be obvious that the fraction of a grid cell occupied by anvil cloud is largely determined by the history of that grid cell, so that a prognostic cloud fraction parameterization is appropriate.

In order to more realistically represent both radiative and microphysical processes in anvil clouds in GCMs, the cloud fraction due to anvil clouds should be included by representing, in a simplified fashion, the physical processes that form, maintain, and dissipate anvil clouds. Such an approach has been developed by Tiedtke (1993) and extended by Randall and Fowler (1999).

3.3 Previous work on cloud ice parameterization

Heymsfield and Donner (1990), Donner et al. (1997), and Köhler (1999), among others, have proposed physically based parameterizations for cirrus cloud properties and/or processes. These investigators have proposed that the properties of cirrus clouds that form *in situ* as a result of large-scale ascent ("large-scale" cirrus) can be largely explained as an approximate balance between ice production by deposition, due to the decrease of saturation mixing ratio, and ice loss due to sedimentation.

In such circumstances, ice production, P, depends primarily on temperature and large-scale vertical velocity, (greater at higher temperatures and for larger vertical velocities), while sedimentation loss, L, depends on the ice mixing ratio, q_i, and the residence time of ice in the layer, τ. The residence time depends on the layer thickness, h, and the ice fall speed, V_i. The result is

$$\frac{dq_i}{dt} = P - L = P - \frac{q_i}{\tau} = P - \frac{q_i V_i}{h}. \tag{49}$$

The steady-state ice mixing ratio is then given by $q_i = P\tau = Ph/V_i$, and therefore depends on several large-scale parameters (temperature, vertical velocity, and cloud thickness) as well as a microphysical parameter (the ice fall speed). This analysis confirms what is well-known from observational studies of cirrus. It also illustrates that a parameterization of cirrus IWC that depends only on temperature is not universal, because IWC depends on (at least) the joint frequency distribution of ice water mixing ratio with temperature, vertical velocity, cloud thickness, and fall speed.

In recent years, many GCMs and NWP models have implemented prognostic cloud water/ice parameterizations, based on equations similar to (49). This should make the dependence of IWC on large-scale processes in such models more realistic. It is also relatively straightforward to include a source due to cumulus detrainment with the prognostic approach.

In the simplest case of anvil cirrus formation and decay, there is no ice production due to large-scale vertical motion. Idealized experiments were performed using the UCLA-University of Utah cloud resolving model (UUU CRM) to study anvil cloud cloud maintenance and decay mechanisms under these conditions (Köhler, 1999). Radiation and turbulence were found to have major effect on the life-time of cirrus clouds. Optically thick ice clouds decay significantly slower than expected from microphysical crystal fall-out due to the upward turbulent flux of water from IR destabilization, which in turn is partially balanced by the downward transport of water by snowfall. Solar radiation further slows the ice water decay by removing the inversion above cloud-top and the increasing the upward transport of water.

Based on the CRM results, Köhler developed an empirical parameterization of the effects of upward turbulent water fluxes in cloud layers by (1) identifying the time-scale of conversion of cloud ice to snow as the key parameter, and (2) regressing it onto cloud differential IR heating and environmental static stability. The results from UCLA GCM simulations showed that artificially suppressing the impact of cloud turbulent fluxes reduces the global mean ice water path by a factor of 3 and produces errors in each of solar and IR fluxes at the top of atmosphere of about 5-6 W m^{-2} (Köhler, 1999). Aircraft measurements also indicate that neglecting the cloud-scale circulations in cirrus clouds may underestimate the grid-averaged IWC by a factor of 2 (Donner et al. 1997).

Köhler did not address the evolution of the fractional area covered by cirrus anvils. Progress on this aspect of anvil cirrus parameterization has been slower than that for the IWC. In order to more realistically represent both radiative and microphysical processes in anvil clouds in GCMs, the cloud fraction due to anvil clouds should be included by representing, in a simplified fashion, the physical processes that form, maintain, and dissipate anvil clouds. Such an approach has been developed by Tiedtke (1993) and extended by Randall and Fowler (1999), but has not been examined using CRMs or tested against observations except indirectly using global, monthly averaged datasets.

3.4 Previous work on cloud fraction parameterization

Tiedtke used the following budget equation for the fractional area of cloud, a, in a grid volume:

$$\frac{\partial a}{\partial t} = A(a) + S(a)_{CV} + S(a)_{BL} + S(a)_C - D(a), \tag{50}$$

where $A(a)$ is the transport of cloud area through the boundaries of the grid volume, $S(a)_{CV}$, $S(a)_{BL}$, and $S(a)_C$ represent the formation of cloud area by cumulus convection, boundary-layer turbulence, and stratiform condensation processes, respectively, and $D(a)$ is the rate of decrease of cloud area due to evaporation.

For completeness, and to aid in the dicussion of anvil cloud processes, we include Tiedtke's budget equation for grid-averaged cloud water/ice content, l:

$$\frac{\partial l}{\partial t} = A(l) + S(l)_{CV} + S(l)_{BL} + S(l)_C - D(l) - G_p, \tag{51}$$

where the terms are analogous to those in Eq (50) except for G_p which is the rate of generation of precipitation from cloud water/ice.

The formation of anvils and cirrus by cumulus convection involve the sources of cloud water content, $S(l)_{CV}$, and cloud area, $S(a)_{CV}$, due to detrainment from cumulus updrafts:

$$S(l)_{CV} = \frac{D_u}{\rho} l_u,$$

$$S(a)_{CV} = (1-a)\frac{D_u}{\rho},$$

where D_u is the rate of detrainment of mass from cumulus updrafts and l_u is the cloud water/ice content in the updrafts. Both D_u and l_u are obtained from the GCM's cumulus parameterization.

Once formed, an anvil or cirrus cloud is subject to non-convective processes, including condensation/deposition due to large-scale ascent, radiative cooling, and turbulent mixing, that tend to increase its area and ice content, and to evaporation and precipitation that tend to decrease its area and ice content.

Based on numerical simulations of cirrus clouds (e.g., Starr and Cox 1985a,b; Fu et al. 1995; Köhler 1999; Luo et al. 2003), the evolution of (thin, non-precipitating) cirrus clouds after their formation by detrainment is governed by the same processes that determine the structure of non-convective ("large-scale") cirrus clouds: large-scale vertical motion, sedimentation and sublimation below cloud base, radiative destabilization, and cloud-scale convective circulations. The role of vertical shear remains uncertain.

There is a great deal of uncertainty in how to represent cloud evaporation/sublimation. Tiedtke proposed that clouds evaporate by two processes: (1) warming due to large-scale descent and/or diabatic heating and (2) (horizontal) turbulent mixing of cloud air and unsaturated environmental air. Tiedtke assumed that the first process decreases the cloud water but does not change the cloud area until the cloud water is gone, and that the second process decreases the cloud area while the in-cloud cloud water content remains unchanged. Randall and Fowler, on the other hand, allow the cloud area to decrease along with the cloud water during the first process, and neglect the second process, but include a diagnosis of subgrid-scale mesoscale vertical motions. Sherwood (1999) suggests that in-cloud radiative warming may drive such mesoscale vertical motions in cirrus clouds, and that the resulting advection of water vapor into the cloudy atmospheric columns may help to sustain the clouds against dissipation.

3.5 Interactions between radiation and convection in tropical cloud clusters

The results of a study of the interactions between radiation and convection in tropical cloud clusters were published in 1995 by Fu et al. (hereafter, FKL95). The goal was to better understand the interactions of infrared (IR) radiation and convection in tropical squall cloud clusters on the time and space scales of an individual cloud system (about 500 km and 12 h). The life cycle of a tropical squall line was simulated over a 12-h period using thermodynamic and kinematic initial conditions as well as large-scale advective forcing typical of a GATE Phase III squall cluster environment.

To study the impact of IR radiation, we performed three simulations: R1, with no radiative cooling; R2, with only clear-sky radiative cooling; and R3, with fully interactive radiative cooling. The differences between R2 and R1 thus represent the effects of *clear-sky IR radiative forcing*, while the differences between R3 and R2 reveal the effects of *IR cloud radiative forcing*. The radiative heating rate profiles for the three simulations are shown in Fig. 3.3.

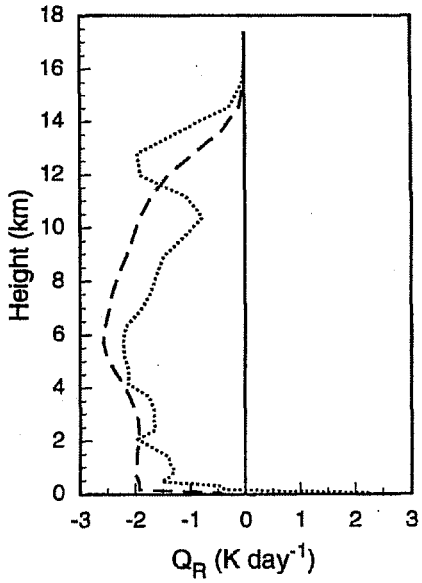

Figure 3.3 The time and domain averaged radiative heating rate profiles for the three simulations (R1, solid; R2, dashed; R3, dotted). [From Fu et al. (1995). Reprinted with permission from the American Meteorological Society.]

The differences between the three simulations are primarily due to the differences in radiative forcing because of the highly organized nature of the simulated convective system. To ensure that such a system developed, the initial wind profile that we used was obtained from a multi-day simulation described in Xu et al. (1992) during a period in which a long-lived squall line developed. In addition, we introduced a cold pool to initiate the squall line. To illustrate the life cycle and structure of a typical simulated convective cloud system, Fig.3.4 shows snapshots of the total hydrometeor mixing ratio, including cloud water, cloud ice, rain, snow, and graupel, based on the R3 simulation at three different times. In the incipient stage (Fig. 3.4a), the cloud system consists of isolated precipitating convective towers. In the mature stage (Fig. 3.4b), new cumulonimbus cells grow at the leading edge

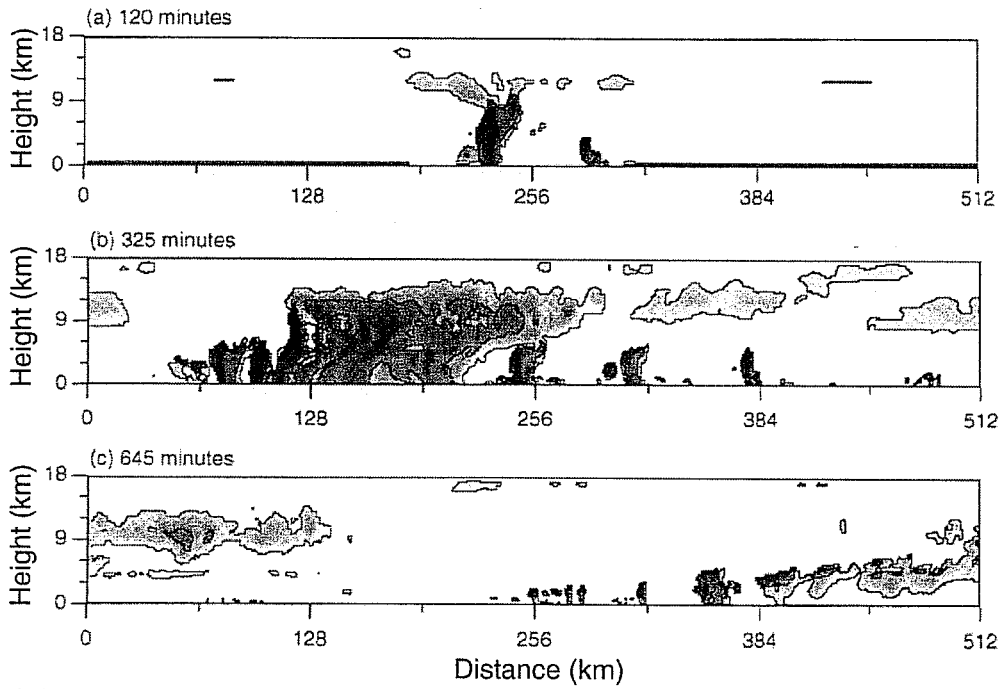

Figure 3.4 Snapshots (x-z sections) of the total hydrometeor mixing ratio, including cloud water, cloud ice, rain, snow, and graupel, based on the R3 simulation at (a) 120, (b) 325, and (c) 645 minutes. The shading is proportional to the logarithm of the mixing ratio: black indicates mixing ratios greater than 10^{-2} and white those less than 10^{-6}. The contours represent mixing ratios of 10^{-4} and 10^{-6}. [From Fu et al. (1995). Reprinted with permission from the American Meteorological Society.]

of the mesoscale convective system, while older cells successively join the anvil cloud, which has a horizontal extent of about 180 km. At this time, significant precipitation covers a region about 140 km wide. In the dissipating stage (Fig.3.4c), little precipitation remains, and the upper-tropospheric stratiform clouds are thinning.

Figure 3.5 illustrates the effects of clear-sky and cloud IR radiative forcing on the surface precipitation rate during simulations R1, R2, and R3. A comparison of R2 and R1 shows that the clear-sky IR radiative forcing increases the surface precipation rate throughout the simulation. A comparison of R3 and R2 shows that the cloud IR radiative forcing has essentially no impact until the time of the peak surface precipitation rate (at 280 min), and acts to decrease the surface precipation rate thereafter. Fig. 3.4c in FKL95 (a time-height cross section of domain-averaged cloud radiative forcing) shows that the cloud radiative forcing does not become significant until about this time. Fig. 3.4 in FKL95 (Hovmuller diagrams of cloud-top temperature for each simulation) shows that significant cloud radiative forcing does not occur until the anvil cloud becomes extensive. The greater extent of the anvil clouds decreases the outgoing IR flux at the top of the atmosphere by as much as 20 W m^{-2}. This figure also shows that the anvil cloud becomes more extensive in R3 than in R2.

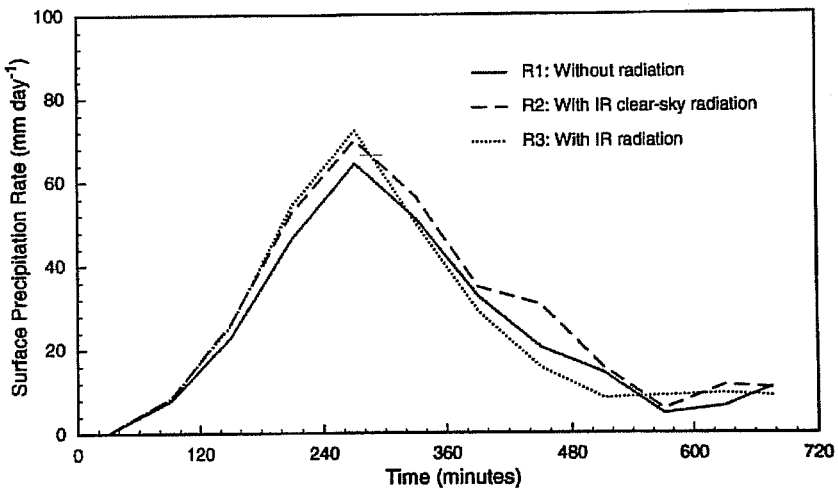

Figure 3.5 Time series of the surface precipitation rate for the three simulations (R1, solid; R2, dashed; R3, dotted)

With fully interactive IR radiative heating, direct destabilization of the anvil clouds via IR cloud-top radiative cooling and cloud-base radiative warming (relative to the clear-sky IR cooling rate; see Fig. 3.3) generates more in-cloud turbulence and contributes to the longevity and extent of the anvil clouds. Fig.3.6 shows that the time and domain averaged cloud fraction at 12 km increases about 0.1 due to cloud radiative forcing, and that this is associated with a marked enhancement of the turbulent kinetic energy within the anvil cloud.

Fig. 3.7 is a schematic illustration of the interactions of IR radiation and convection examined in FKL95's study. It shows that IR clear-sky radiation tends to destabilize the troposphere by cooling it, while IR cloud radiative forcing (due to the radiative effects of the anvil cloud) tends to stabilize the troposphere below 10 km by warming it (relative to IR clear-sky cooling). IR cloud radiative forcing also tends to destabelize the anvil cloud layer from 10 to 14 km, which thereby increases the extent and longevity of the anvil clouds, and thus feeds back to the IR cloud radiative forcing.

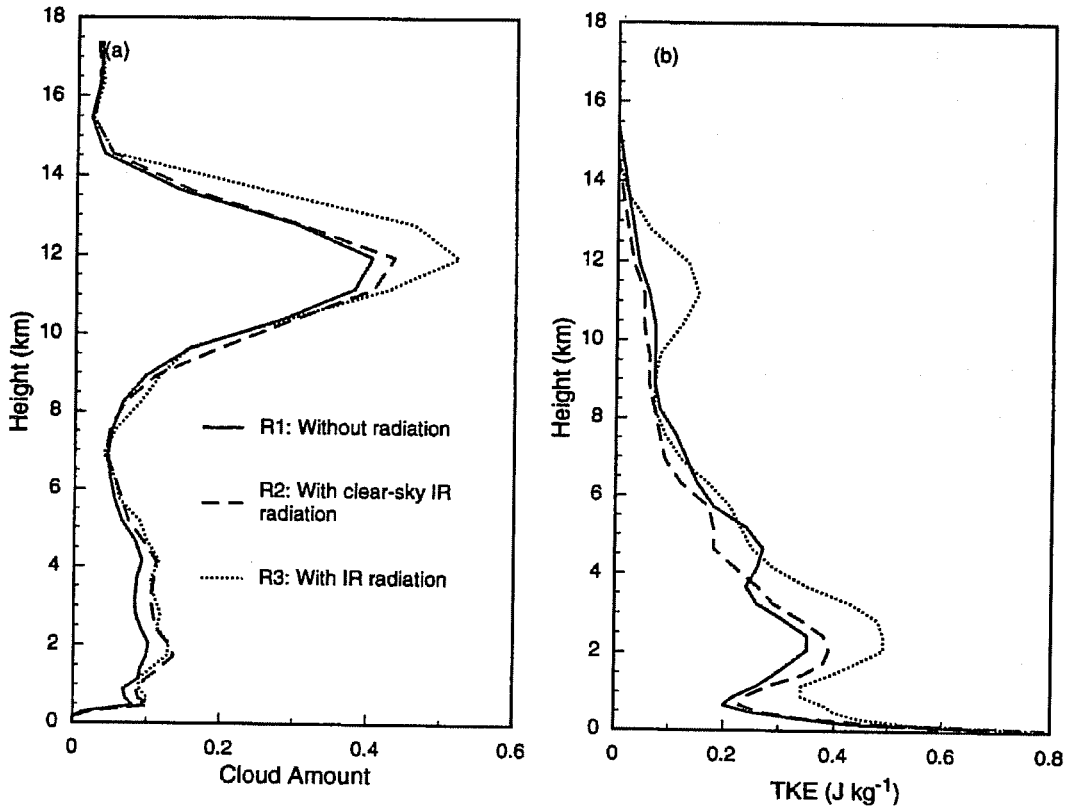

Figure 3.6 The time and domain averaged (a) cloud fraction and (b) turbulent kinetic energy (TKE) profiles for the three simulations. [From Fu et al. (1995). Reprinted with permission from the American Meteorological Society.]

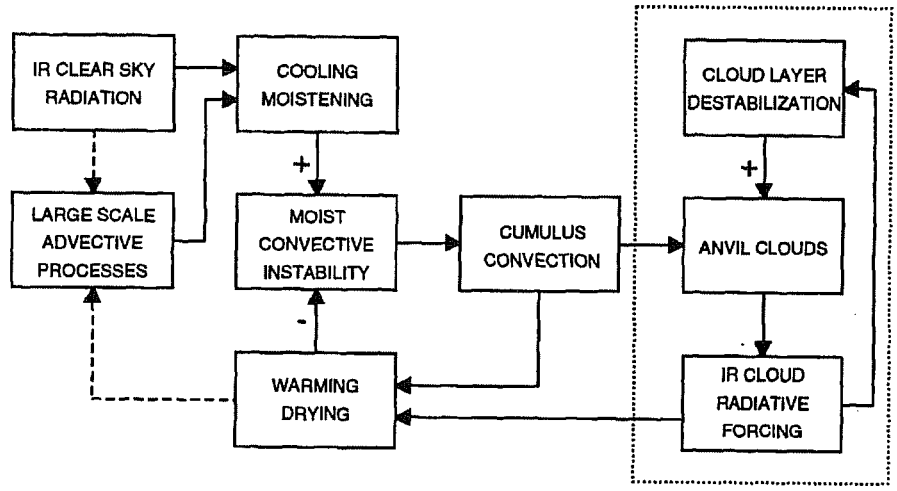

Figure 3.7 A schematic illustration of the mesoscale interactions of IR radiation and convection. The dashed lines indicate large-scale feedbacks that are not included in the CEM simulations. [From Fu et al. (1995). Reprinted with permission from the American Meteorological Society.]

4. Diurnal cycle of deep cumulus convection

Analysis of the diurnal cycle represents a powerful tool for identifying and correcting model deficiencies (e.g., Lin et al. 2000; Yang and Slingo 2001). Several global observational datasets are now available for such purposes (e.g., Yang and Slingo 2000; Nesbitt and Zipser 2002). Lin et al. compared observations from several such datasets with the diurnal variability of the Amazonian hydrologic cycle and radiative energy budget as simulated

by the Colorado State University general circulation model to evaluate improvements and deficiencies of the model physics. The model uses a prognostic cumulus kinetic energy (CKE) to relax the quasi-equilibrium closure of the Arakawa-Schubert cumulus parameterization. A parameter is used to relate the CKE to the cumulus mass flux. This parameter is expected to vary with cloud depth, mean shear, and the level of convective activity, but up to now a single constant value for all cloud types has been used. The results of their study show clearly that this approach cannot yield realistic simulations of both the diurnal cycle and the monthly mean climate state. Improved results are obtained using a version of the model in which the parameter is permitted to vary with cloud depth.

A global archive of high-resolution IR window brightness temperature data from multiple satellites is being developed by the European Union Cloud Archive User Service (CLAUS) project. Yang and Slingo (2001) used it to construct a climatology of the diurnal cycle in convection, cloudiness, and surface temperature for all regions of the Tropics. They also applied the climatology to the evaluation of the climate version of the U.K. Met. Office Unified Model (UM), version HadAM3.

This example demonstrated that the model has considerable difficulty in capturing the observed phase of the diurnal cycle in convection, which suggests some fundamental difficulties in the model's physical parameterizations.

In the remainder of this section, I will briefly describe the diurnal cycle of rainfall and convective intensity according to three years of Tropical Rainfall Measurement Mission (TRMM) measurements. Nesbitt and Zipser (2002) combined TRMM satellite measurements from the Precipitation Radar (PR) and TRMM Microwave Imager (TMI) to yield a three-year database of precipitation features (PFs) throughout the global tropics (± 36 degrees latitude). This database includes a sample of nearly six million. The PFs retrieved using this algorithm were sorted by size and intensity, ranging from small shallow features to large mesoscale convective systems (MCSs), according to their radar and ice scattering characteristics. Unlike previous studies which rely on indirect proxies like IR brightness temperatures to estimate the diurnal cycle, TRMM allows a much more direct measurement of the near surface rainfall rate using a radar reflectivity-rainfall rate algorithm.

In addition, the diurnal cycle of convective intensity can be estimated by the characteristics of each PF measured by the PR and TMI: specifically, the minimum 85 and 37 GHz Polarization Corrected Temperatures and the maximum heights of the 30 and 40 dBZ echoes. Many studies have linked these characteristics to updraft intensity. Radiative transfer calculations indicate that brightness temperature depressions at 85 GHz are most sensitive to scattering by precipitation-sized ice particles greater than a few hundred micrometers in size, while depressions at 37 GHz require significant concentrations of particles with radii greater than roughly millimeter-size.

These observations have been sorted geographically to examine the differences in the diurnal cycle of volumetric rainfall rate and convective intensity over land and ocean areas. The volumetric rainfall is the product of the mean conditional rain rate, the mean area, and the total number of features. The conditional rain rate is the average rainfall rate within a PF. Figures 4.1 and 4.2 show the diurnal cycles for all four of these quantities for all 3 PF types.

Figure 4.1 shows that over the oceans, the diurnal cycle of rainfall rate has a significant amplitude (15 percent of the mean rate) with the maximum contribution to rainfall rate coming from MCSs in the early morning. This increased contribution is due to an increased number of MCSs in the nighttime hours, not increased MCS areas or conditional rain rates. Sub-MCS features display no appreciable diurnal cycle of rainfall rate or convective intensity.

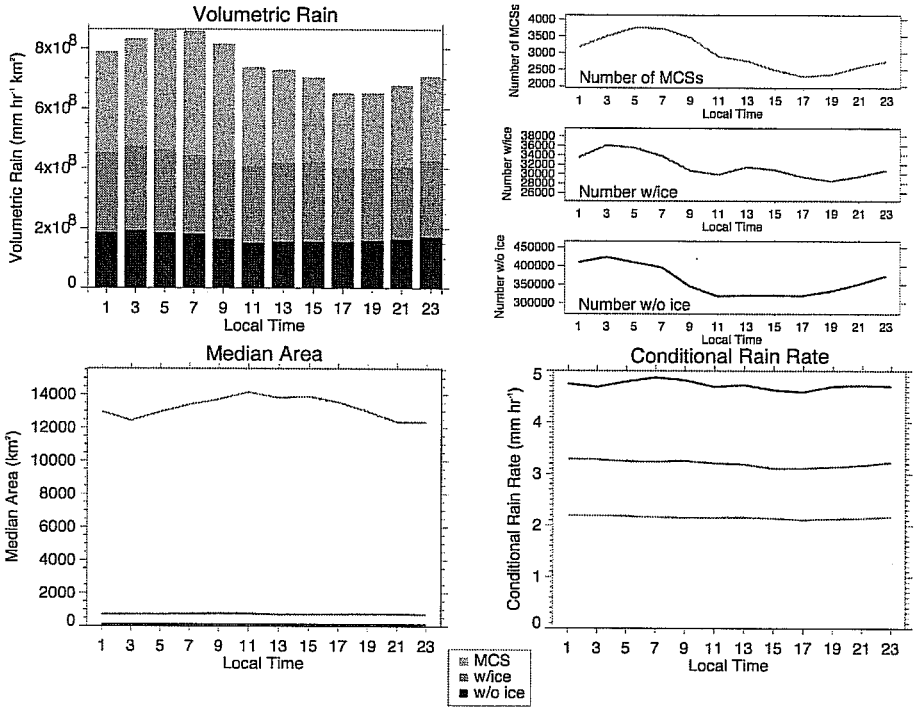

Figure 4.1 Fraction of grid cells that are convective grid cells for horizontal grid sizes from 2 km to 256 km.

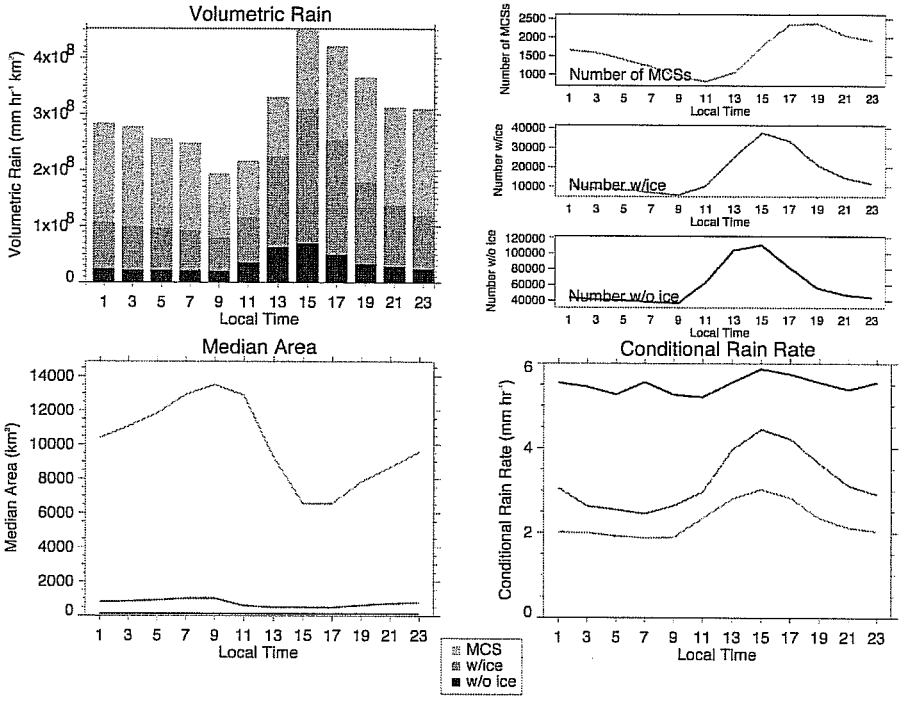

Figure 4.2 Resolved non-convective mass flux, for horizontal grid sizes from 2 km to 256 km

Previous theories on diurnal cycle mechanisms suggested that conditional rain rates are heavier during the observed pre-dawn maximum of oceanic rainfall rate. Nesbitt and Zipser see little enhancement in the observed convective intensities and conditional rain rates that correspond with the observed pre-dawn increase in rainfall rate. The larger number of systems observed during the pre-dawn hours suggests that over the ocean, the nocturnal

environment is simply more favorable for cloud systems to grow to become MCSs, or for MCSs to persist. (The snapshots from TRMM do not allow the system life cycle to be directly observed).

As shown in Fig. 4.2, the amplitude of the diurnal cycle of rainfall rate over the continents is 60 percent of the mean rate, which is much larger than over the oceans. The continental rainfall rate has a marked minimum in the midday hours and a maximum in the afternoon, slowly decreasing through midnight. MCSs over land have a convective intensity peak in the late afternoon. However, all land regions have MCS rainfall peaks that occur in the around midnight. The number of systems, rainfall rates, and convective intensities of sub-MCS features respond strongly to afternoon heating. MCSs over land also see an increase in conditional rain rates and convective intensities in the afternoon; however their persistence and increasing areas throughout the nighttime lead to a near-midnight maximum in MCS rainfall. The mechanisms of the rainfall peak associated with afternoon instability over land are well understood and observed. However, the diurnal cycle of rainfall associated with continental MCSs remains poorly understood.

The TRMM PF database is well-suited for evaluating the performance of cloud-resolving models (CRMs) on a statistical basis as well as the performance of global circulation models (GCMs). Future work with this comprehensive dataset will include detailed comparisons with CRMs and GCMs.

5. Mesoscale cumulus parameterization

The horizontal grid size in NWP models will continue to decrease. For example, it is now 40 km in the ECMWF model, and even less in many regional models. There are many reasons to decrease the horizontal grid size in LSMs. In general, as the grid size decreases, small-scale processes become better resolved so that the need to parameterize subgrid-scale processes also decreases. Stratiform cloud formation is one example. As the grid size decreases, the cloud fraction (i.e., cloud amount at a given level) tends towards a bimodal, 0 or 1, distribution, as shown in Table 1, which reduces the need to parameterize cloud fraction and cloud overlap.

grid size (km)	clear frequency (%)	overcast frequency (%)
512	22	8
256	28	9
128	36	12
64	44	17
32	49	22
16	55	29

Table 1 Frequency of occurrence of clear (cirrus cloud amount < 5%) and overcast (cirrus cloud amount > 95%) conditions versus horizontal grid size, as simulated by a cloud resolving model with 2-km horizontal grid size. The average cirrus cloud amount was 38%.

In particular, as the grid size decreases, the processes that determine the location, timing, and intensity of convective rainfall should become better resolved, which should improve forecasts of convective precipitation. Triggering of convection will be better represented, due to increased resolution of mesoscale boundary-layer circulations, such as sea breezes, orographic circulations, and convective outflows.

As the horizontal grid size decreases, many of the processes that determine the structure of mesoscale convective systems (MCSs) will also be better resolved. These processes include the interaction of vertical shear of the lower

tropospheric horizontal wind with cold pools produced by evaporation of convective precipitation. This process is important for the formation and longevity of some types of squall lines (Rotunno et al. 1988).

However, until horizontal grid sizes decrease to 4 km or less, cumulus convection will still need to be parameterized (Weisman et al. 1997). As horizontal grid sizes decrease, parameterized convection becomes more localized. That is, a smaller fraction of the grid columns are *convective columns* (i.e., columns that contain areas of cumulus convection) and these columns include larger fractional areas of cumulus convection. What are the implications for cumulus parameterization as horizontal grid size decreases and convection becomes more localized? Can we quantify the implications? Do some aspects of the cumulus parameterization for large-scale models described in section 2 become inappropriate as horizontal grid size decreases? If so, which ones?

The basic idea of a LSM cumulus parameterization is that a grid column contains an ensemble of cumulus clouds and that the fractional area covered by the active cumulus updrafts is small. In this case, the primary large-scale effects of the cumulus ensemble, heating and drying due to cumulus-induced subsidence and moistening due to cumulus detrainment, are assumed to be distributed over the area of the grid column. In reality, the subsidence would spread over a Rossby radius of deformation. However, the horizontal variations of cumulus ensemble activity are assumed to be small because horizontal grid size is assumed to be much smaller than the size of large-scale disturbances. In addition, the horizontal grid size is large enough so that the parameterized cumulus convection is not localized. In effect, it is assumed that there are only two scales: cumulus scale and large scale, with a clear separation between them.

As the grid size decreases and the mesoscale is resolved, the scale separation between resolved scales and cumulus scale becomes indistinct. However, if the cumulus parameterization problem is recast to one of localizing the convection, but still determining its intensity based on the closure principles used for LSM cumulus parameterization, the problem may be simpler and more tractable. The basis for this is the observation that, although the cumulus updrafts are localized, dry adjustment quickly distributes their subsidence effects over a large-scale area (a Rossby radius of deformation).

If a goal of reducing the horizontal grid size is to improve convective precipitation forecasts, then one must more accurately predict the occurrence of mesoscale convective systems (MCSs). To do this requires parameterizing the cumulus heating so that it resembles the actual mesoscale patterns of time-averaged convective heating (Pandya and Durran 1996). It also appears necessary to detrain a fraction of the parameterized cloud and precipitation particles to the grid scale to allow explicit calculation of the slow hydrometeor growth, fallout, and phase changes that are characteristic of MCSs (Molinari and Dudek 1992).

Finally, the localization of parameterized convection in mesoscale models will make initiation or "triggering" of convection an important issue. The most difficult aspect of convection initiation seems to be predicting the first convective event in a region because it will by definition be triggered by a non-convective boundary layer convergence zone. The occurrence of such convergence zones is very difficult to predict.

We used the results of a 29-day, 2D CRM simulation of mostly deep convective cloud systems over Oklahoma during the summer to quantify the dependence of some aspects of cumulus parameterization on horizontal grid size, at a single level (4.2 km MSL). The CRM's horizontal grid size was 2 km, so that it resolved both the cloud-scale and the mesoscale vertical motions associated with deep convective cloud systems. The cloud-scale vertical motions consist of strong and narrow cloudy updrafts and precipitation-driven downdrafts; they comprise the *convective* portions of a deep convective cloud system. The mesoscale vertical motions consist of broader and

slower updrafts and downdrafts associated with the *stratiform* precipitation regions of a deep convective cloud system.

A mesoscale cumulus parameterization attempts to determine the characteristics of the convective portions of a deep convective cloud system. We identified the *convective grid columns* in the CRM simulation using the method of Xu (1995). The convective grid columns are the convective portions of the simulated deep convective cloud systems. Here, a *grid column* refers to an actual grid column in the CRM. A *grid cell* will refer to a hypothetical grid column in a mesoscale or large-scale model; we considered grid cells with horizontal grid sizes that range from 2 km to 256 km. A *convective grid cell* contains at least one *convective grid column.*

The convective grid cell fraction, $f_c(\Delta x)$, is the fraction of grid cells with horizontal grid size equal to Δx that are convective grid cells, when there is at least one convective grid cell in the CRM's 512-km horizontal domain. Figure 5.1 shows that f_c increases from 0.07 for Δx = 2 km to 0.80 for Δx = 256 km. The relationship is approximately

$$f_c(\Delta x) = 0.8\left(\frac{\Delta x}{256\text{km}}\right)^{1/2},$$

for Δx in km. The total number of grid columns per unit area is proportional to $(\Delta x)^{-2}$. Thus, the number of *convective grid cells per unit area* is proportional to $(\Delta x)^{3/2}$.

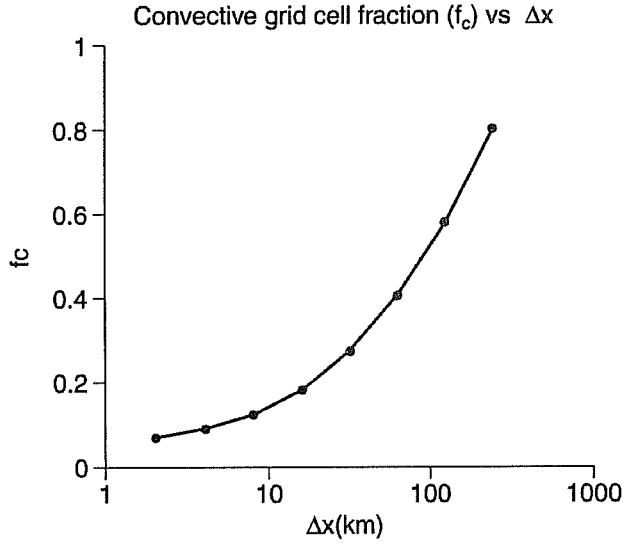

Figure 5.1 Fraction of grid cells that are convective grid cells for horizontal grid sizes from 2km to 256km.

Let w be the departure of the vertical velocity from the large-scale average vertical velocity, $w(\Delta x)$ be w averaged over a horizontal distance Δx, and $\overline{w}_c(\Delta x)$ represent the large-scale average of $w(\Delta x)$ over all grid cells of size Δx that are convective. Similarly, let $\overline{w}_n(\Delta x)$ refer to $w(\Delta x)$ averaged over all non-convective grid cells, and $\overline{w}(\Delta x)$ to $w(\Delta x)$ averaged over all grid cells. By the definition of $\overline{w}(\Delta x) = 0$. It follows that

$$\overline{w}(\Delta x) = f_c(\Delta x)\overline{w}_c(\Delta x) + \left[1 - f_c(\Delta x)\right]\overline{w}_n(\Delta x) = 0$$

Figure 5.2 shows that the *resolved convective mass flux*, $\rho\overline{w}_c(\Delta x)$ increases rapidly as Δx falls below 32 km. Figure 5.3 shows that the *resolved non-convective mass flux*, $\rho\overline{w}_n(\Delta x)$, increases slowly in magnitude as Δx falls below 16 km. To convert the mass fluxes into vertical velocities, divide by the density (0.77 kg m^{-3}).

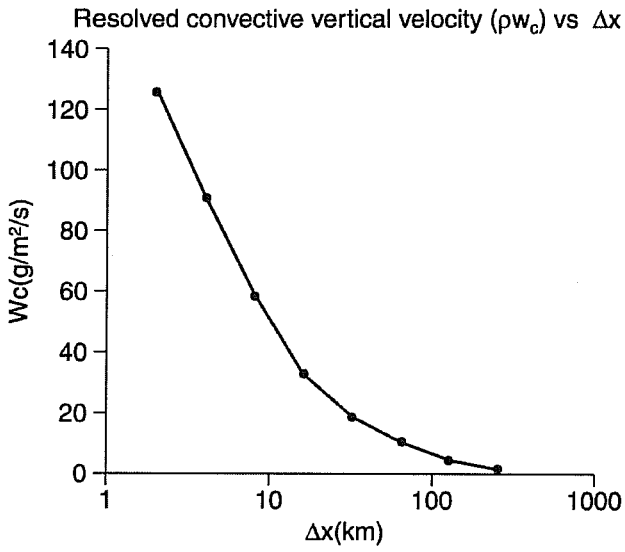

Figure 5.2 Resolved fraction of convective circulation for horizontal grid sizes from 2km to 256km

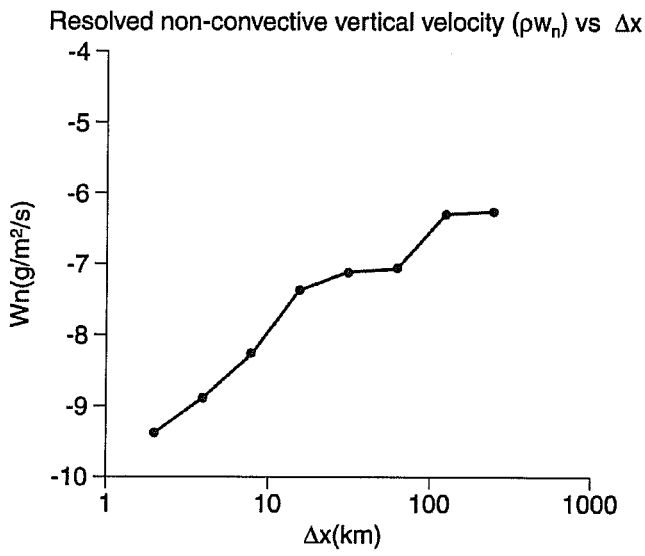

Figure 5.3 Resolved non-convective mass flux, for horizontal grid sizes from 2km to 256km

The net upward *cumulus mass flux* at a given level is

$$M_c = \int \rho w \, d\sigma,$$

where

$$\sigma = \int d\sigma$$

is the fraction of the large-scale area covered by active cumulus clouds. We will approximate the area covered by active cumulus clouds by the area occupied by the convective grid columns. Then

$$\sigma = f_c(2\text{km})$$

$$M_c = \rho f_c(2\text{km}) \overline{w}_c(2\text{km})$$

because for Δx = 2 km, each convective grid cell is a convective grid column. Similarly, the compensating subsidence due to cumulus convection is

$$\tilde{M} = -M_c$$

Figure 5.2 shows that as $\Delta x \to 512$ km, $\rho \overline{w}_c(\Delta x) \to 0$, which implies that the compensating subsidence occurs increasingly within the convective grid cells. Conversely, as $\Delta x \to 0$, the active cumulus clouds (convective grid columns) and compensating subsidence tend to occur in different grid cells, and $\rho \overline{w}_c(\Delta x)$ increases toward the limiting value of

$$\rho \overline{w}_c(2\text{km}) = \frac{M_c}{\sigma}$$

This suggests that we define the *resolved cumulus mass flux* as

$$\hat{M}_c(\Delta x) = \rho f_c(\Delta x) \overline{w}_c(\Delta x).$$

The *resolved compensating subsidence* is then $-\hat{M}_c(\Delta x)$.

As $\Delta x \to 0$ km, $\hat{M}_c \to M_c$ as the convective circulation becomes increasingly resolved. What is the fraction of the convective circulation that is resolved into its ascending and descending branches by the convective grid cells, as a function of grid cell size? It is

$$\frac{\hat{M}_c(\Delta x)}{M_c}$$

which is shown in Fig.5.4.

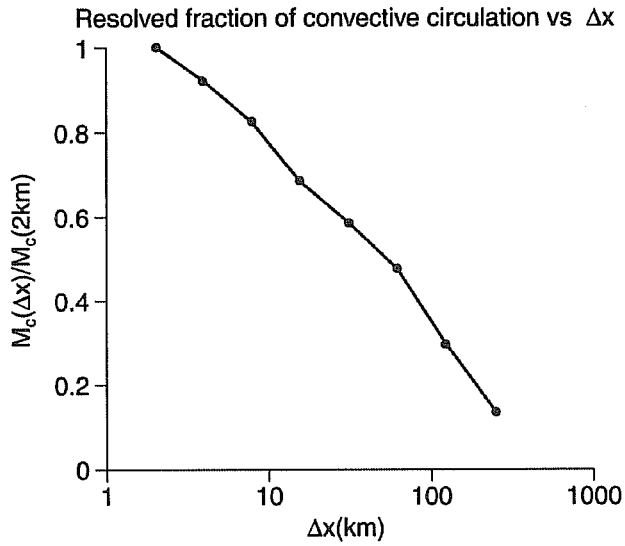

Figure 5.4 Resolved fraction of convective circulation for horizontal grid sizes from 2km to 256km

As $\Delta x \to 512$km, $\hat{M}_c \to 0$ as the convective circulation becomes increasingly subgrid-scale. What is the fraction of the convective circulation that is subgrid-scale (that is, occurs entirely within the convective grid cells) as a function of grid cell size?

It is

$$\frac{M_c - \hat{M}_c(\Delta x)}{M_c} = 1 - \frac{\hat{M}_c(\Delta x)}{M_c}.$$

This is shown in Fig. 5.5.

An important question for mesoscale cumulus parameterization is: How does the *average convective column fraction* in the convective grid cells depend on Δx? Let $\alpha(\Delta x)$ be the average convective column fraction in the convective grid cells, w_u the average w in convective *columns*, and w_d the average w in non-convective *columns*. Then

$$\rho\overline{w}_c(\Delta x) = \rho\alpha(\Delta x)w_u + \rho[1-\alpha(\Delta x)]w_d$$

Note that w_u and w_d are independent of Δx:

$$w_u = \overline{w}_c(2\text{km})$$

$$w_d = -\frac{\sigma}{1-\sigma} w_u$$

and

$$\sigma = f_c(2\text{km})$$

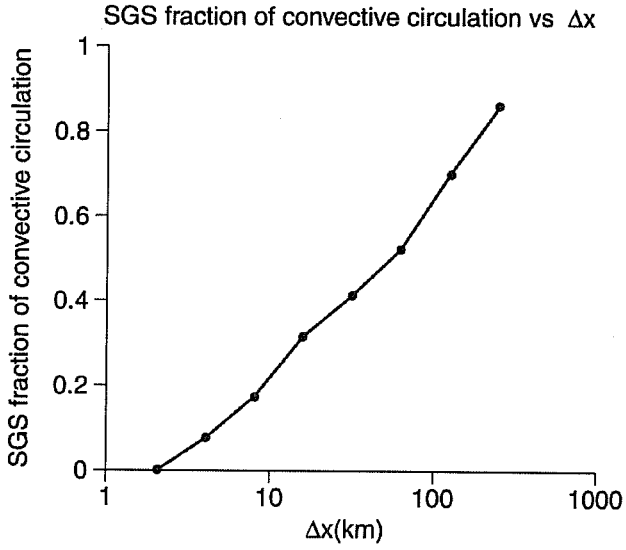

Figure 5.5 Subgrid-scale fraction of convective circulation for horizontal grid sizes from 2 km to 256 km.

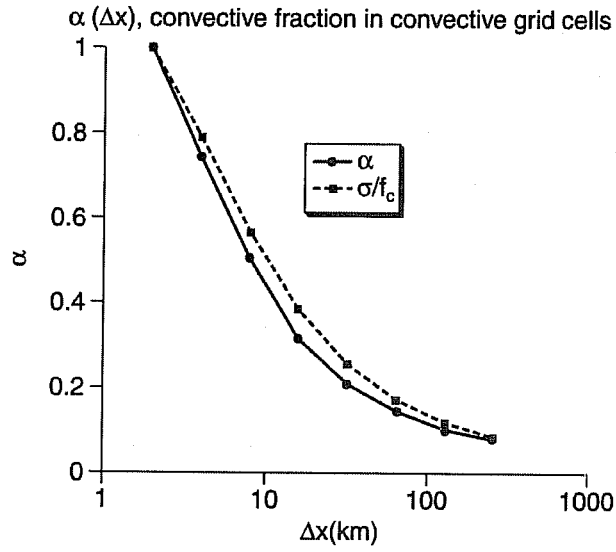

Figure 5.6 Average convective column fraction in the convective grid cells for horizontal grid sizes from 2 km to 256 km.

From these relations, we can solve for $\alpha(\Delta x)$ in terms of $\overline{w}_c(\Delta x)$:

$$\alpha(\Delta x) = \frac{\dfrac{\overline{w}_c(2\text{km})}{w_u} + \gamma}{1+\gamma},$$

where

$$\gamma \equiv \frac{\sigma}{1+\sigma}.$$

An approximate relation between α and f_c is

$$\alpha(\Delta x) \approx \frac{\alpha}{f_c(\Delta x)}.$$

Both of these expressions for $\alpha(\Delta x)$ are shown in Fig. 6, which shows that α increases rapidly as Δx decreases below 64 km.

References

Arakawa, A., and W. H. Schubert, 1974: Interaction of a cumulus cloud ensemble with the large-scale environment. Pt. I. *J. Atmos. Sci.*, **31**, 674-701.

Donner, L. J., Seman, C. J., Soden, B. J., Hemler, R. S., Warren, J. C., Strom, J., and Liou, K.-N., 1997: Large-scale ice clouds in the GFDL SKYHI general circulation model. *J. Geophys. Res.*, **102**, 21745-21768.

Fu, Q., S. K. Krueger, and K.N. Liou, 1995: Interactions of radiation and convection in simulated tropical cloud clusters. *J. Atmos. Sci.*, **52**, 1310-1328.

Heymsfield, A. J., and L. J. Donner, 1990: A scheme for parameterizing ice-cloud water content in general circulation models. *J. Atmos. Sci.*, **47**, 1865-1877.

Houze, R. A., Jr., 1977: Structure and dynamics of a tropical squall-line system. *Mon. Wea. Rev.*, **105**, 1540-1567.

Köhler, M., 1999: Explicit prediction of ice clouds in general circulation models. *Ph. D. dissertation, University of California, Los Angeles*, 167 pp.

Lau, N.-C., and Crane, M. W., 1995: A satellite view of the synoptic-scale organization of cloud properties in midlatitude and tropical circulation systems. *Mon. Wea. Rev.*, **123**, 1984-2006.

Lau, N.-C., and Crane, M. W., 1997: Comparing satellite and surface observations of cloud patterns in synoptic-scale circulation systems. *Mon. Wea. Rev.*, **125**, 3172-3189.

Leary, C. A., and Houze, R. A., Jr., 1979: Structure and evolution of convection in a tropical cloud cluster. *J. Atmos. Sci.*, **36**, 437-457.

Lord, S. J., and A. Arakawa, 1980: Interaction of a cumulus cloud ensemble with the large-scale environment, Pt. II. *J. Atmos. Sci.*, **37**, 2677-2692.

Luo, Y., S. K. Krueger, G. G. Mace, and K.-M. Xu, 2003: Cirrus cloud properties from a cloud-resolving model simulation compared to cloud radar observations. *J. Atmos. Sci.*, **60**, in press.

Machado, L. A. T., and Rossow, W. B., 1993: Structural characteristics and radiative properties of tropical cloud clusters. *Mon. Wea. Rev.*, **121**, 3234-3260.

Molinari, J., and Dudek, M., 1992: Parameterization of convective precipitation in mesoscale numerical models: a critical review. *Mon. Wea. Rev.*, **120**, 326-344.

Pandya, R., and Durran, D. R., 1996: The influence of convectively generated thermal forcing on the mesoscale circulation around squall lines. *J. Atmos. Sci.*, **53**, 2924-2951.

Randall, D. A., and L. D. Fowler, 1999: Eauliq: The Next Generation. *Atmospheric Science Paper* No. 673, Colorado State University, 65 pp.

Rotunno, R., Klemp, J. B., and Weisman, M. L. , 1988: Theory for strong, long□lived squall lines. *J. Atmos. Sci.*, **45**, 463-485.

Sherwood, S. C., 1999: On moistening of the tropical troposphere by cirrus clouds. *J. Geophys. Res.*, **104**, 11,949-11960.

Starr, D. O'C., and S. K. Cox, 1985a: Cirrus clouds. Part I: A cirrus cloud model. *J. Atmos. Sci.*, **42**, 2663-2681.

Starr, D. O'C., and S. K. Cox, 1985b: Cirrus clouds. Part II: Numerical experiments on the formation and maintenance of cirrus. *J. Atmos. Sci.*, **42**, 2682--2694.

Tiedtke, M., 1993: Representation of clouds in large-scale models. *Mon. Wea. Rev.*, **121**, 3040-3061.

Weisman, M. L., Skamarock, W. C., and Klemp, J. B., 1997: The resolution dependence of explicitly modeled convective systems. *Mon. Wea. Rev.*, **125**, 527-548.

Xu, K.M., 1995: Partitioning mass, heat, and moisture budgets of explicitly simulated cumulus ensembles into convective and stratiform components. *J. Atmos. Sci.*, **52**, 551-573.

Xu, K.-M., A. Arakawa, and S.K. Krueger, 1992: The macroscopic behavior of cumulus ensembles simulated by a cumulus ensemble model. *J. Atmos. Sci.*, **49**, 2402-2420.